Explicit failure model for boron carbide ceramics under shock loading

S. A. Dyachkov, A. N. Parshikov, M. S. Egorova, S. Yu. Grigoryev, V. V. Zhakhovsky, and S. A. Medin

---

Articles you may be interested in

Ejecta from shocked metals: Comparative simulations using molecular dynamics and smoothed particle hydrodynamics
AIP Conference Proceedings **1793**, 100024 (2017); 10.1063/1.4971649

Explicit failure model for boron carbide ceramics under shock loading

S. A. Dyachkov,[1,2,3,4,a)] A. N. Parshikov,[1,3,b)] M. S. Egorova,[1,4] S. Yu. Grigoryev,[1,4]
V. V. Zhakhovsky,[1,4] and S. A. Medin[2,3]

[1]*Dukhov Research Institute of Automatics, 22 Sushchevskaya st., Moscow 127055, Russia*
[2]*Moscow Institute of Physics and Technology (State University), 9 Institutskii per., Dolgoprudny, Moscow Region 141701, Russia*
[3]*Joint Institute for High Temperatures, 13 bd. 2 Izhorskaya st., Moscow 125412, Russia*
[4]*Landau Institute for Theoretical Physics, 1-A Akademika Semenova av., Chernogolovka, Moscow Region 142432, Russia*

Ceramic materials have a long-term industrial demand due to their high mechanical hardness and chemical and temperature resistance. They are brittle and tend to lose strength under heavy loads which complicates the development of a comprehensive material model for simulation of engineering prototypes containing ceramic parts. We developed an improved failure model of ceramics based on the well-known Johnson–Holmquist approach. This model redefines the damage rate equation using a consistent definition of the total plastic strain in the failed material. It reduces the number of free model parameters and enables the plastic strain to be explicitly accumulated during the failure process. The corresponding non-iterative algorithm utilizing this explicit failure model is developed. It is successfully validated by simulation of the wave profiles obtained in plate-impact experiments with boron carbide using the contact smoothed particle hydrodynamic method. *Published by AIP Publishing.* https://doi.org/10.1063/1.5043418

I. INTRODUCTION

Boron carbide has widespread applications due to its unique mechanical and thermal properties, which is why this material has been studied extensively both on micro- and macro-scales.[1] This material is lightweight ceramic with a normal density of about 2.52 g/cm^3, which has the relatively high melting point of about 2450 K and the highest Hugoniot Elastic Limit (HEL) of about 15–18 GPa among all other ceramics. Having considerable strength, boron carbide is usually applied as an abrasive and impact protection material. The boron ability for neutron absorption is also a demanded feature in the nuclear industry.

To study the response of boron carbide to extreme conditions produced at high impact velocity, many shock compression experiments were performed.[2] The observed material failure produced by shock loading manifests itself as a sharp decline of shear strength of the material. Such failure takes place just behind a shock front in other similar ceramics such as silicon carbide.[3] The same behavior of boron carbide is also observed in various experiments.[4–11]

Atomistic mechanisms leading boron carbide to a failure state under shock compression are not clarified yet.[2,12] High-resolution electron microscopy of boron carbide fragments in the ballistic experiment[13] revealed the formation of multiple intragranular amorphous bands. Similar structures appear in a uniaxially compressed boron carbide sample placed in a diamond anvil cell (DAC) during stress unloading from 50 GPa.[14] State-of-the-art annular bright-field scanning transmission electronic microscopy[15] revealed the structure of amorphous shear bands: they result from the disassembly of the 12-atom icosahedra, driven by shear stresses. Nevertheless, the volumetric compression in DAC[16] does not show any non-monotonic changes up to 74 GPa. These facts lead to a hypothesis that non-hydrostatic compression is required to trigger the amorphization and drop of material strength.

The above experimental observations inspired several ab-initio studies aiming to reveal the failure mechanism on atomic scales. The original hypothesis[14] was that the discontinuous volume change appears due to C-B-C chain bending; however, the obtained amorphization stresses are varied much in different predictions.[14,17,18] The main reason for these variations could be because the different stoichiometries were used.[19] Moreover, the vacancy in a chain (C-V-C) could also be responsible for the experimentally observed amorphization pressure threshold of ∼25 GPa.[20] The mechanisms of chain bending are analyzed in different loading conditions[21–23] which are also essential for the resulting amorphization stress magnitude. The simulation of shear stress induced amorphization using the ab-initio and reactive force field molecular dynamics[24] revealed that amorphous boron carbide has a higher density than the crystal material. Another failure mechanism can be realized at boron carbide grain boundaries.[25]

Modeling of engineering prototypes containing elements from boron carbide is in demand, which is why various failure models are in active development. Nowadays, Johnson–Holmquist (JH-1[26] and JH-2[27]) and Johnson–Holmquist–Beissel (JHB[28]) models with the many empirically fitted parameters[29,30] are widely used for boron carbide. The basis for both models is the observed fact of strength loss under loading. HEL corresponds to the intact strength limit σ_i, beyond which the failure process is initiated. As this takes

a)Electronic mail: sergei.dyachkov@phystech.edu
b)Electronic mail: anatoliy.parshikov@gmail.com

place, the stress-strain characteristics of ceramics change so that the strength limit reduces from the initial one to some minimal value—the strength of the completely failed material σ_f. The model transformation from intact to a failed state may be instantaneous (JH-1 and JHB) or gradual (JH-2) where a material state is described using the damage degree parameter $D \in [0, 1]$. This parameter increases with time via accumulation of plastic strain, which is defined as a difference between the total strain (from a solution of the continuity equation) and elastic strain.

Implementation of the JH-1, JH-2, and JHB models can be unfeasible in-house for the lack of details in the published articles. In particular, an algorithm of plastic strain accumulation and a ready-to-implement ceramic failure model are rarely provided in a comprehensive form. Our work describes a ceramic failure algorithm in detail enough to be programmed straightforwardly.

Here, we introduce a new method for plastic strain accounting and provide its validation on two experimental sets.[8,9] The controversial structural phase transition, which is supposed to be at about 40 GPa, is not included in our model because there is no evidence for that in DAC experiments.[14,16] Instead, the local structural changes in the damaged material are considered as the consequences of amorphization under shock loading. The maximal plastic strain corresponding to the failed state of boron carbide is defined via the difference between the intact and failed strengths, which sets the model up with an extra consistency. Material modeling is performed here using the contact Smoothed Particle Hydrodynamic (cSPH) method,[31] but the model is useful for any discrete representation of the material because it describes a local damage process in each element independently.

II. EQUATIONS OF MOTION FOR THE ELASTO-PLASTIC MATERIAL

Deformation and motion of a continuous material in numerical modeling are guided by the conservation laws for the mass, momentum, and energy given by

$$\dot{\rho}/\rho = -\dot{\theta} = -\nabla \cdot \mathbf{U}, \tag{1}$$

$$\rho\dot{\mathbf{U}} - \nabla \cdot \boldsymbol{\sigma} = 0, \tag{2}$$

$$\rho\dot{E} - \nabla \cdot (\boldsymbol{\sigma} \cdot \mathbf{U}) = 0. \tag{3}$$

Here, the Lagrangian formulation is used, wherein ρ and $\mathbf{U}$ are the density and velocity of a material element, respectively; the total energy $E = e + \mathbf{U}^2/2$ per unit mass consists of the internal and kinetic energies, and $\boldsymbol{\sigma}$ is the total stress tensor defined as

$$\boldsymbol{\sigma} = -P(\rho, e)\mathbf{I} + \mathbf{S}, \tag{4}$$

where P is the pressure determined through an equation of state, $\mathbf{S}$ is the elastic stress deviator, and $\mathbf{I}$ is the second-rank unit tensor. The stress deviator in the elastic material with accounting of rotation is given by Hooke's law

$$\dot{\mathbf{S}} = 2G(\dot{\boldsymbol{\varepsilon}} - \dot{\boldsymbol{\varepsilon}} \otimes \mathbf{I}/3) - \dot{\mathbf{R}} \cdot \mathbf{S} + \mathbf{S} \cdot \dot{\mathbf{R}}, \tag{5}$$

where G is the shear modulus and $\dot{\mathbf{R}}$ is the angular velocity tensor which is given by

$$\dot{\mathbf{R}} = \left[(\nabla \otimes \mathbf{U})^{\mathrm{T}} - \nabla \otimes \mathbf{U}\right]/2. \tag{6}$$

The components of the volumetric strain rate tensor can be found from the Saint-Venant's compatibility condition

$$2\dot{\boldsymbol{\varepsilon}} - \nabla \otimes \mathbf{U} - (\nabla \otimes \mathbf{U})^{\mathrm{T}} = 0. \tag{7}$$

The system of mechanical equations (1)–(6) must be completed by the thermodynamic equation of state that provides a relationship between pressure P, density ρ, and internal energy e

$$P = P(\rho, e). \tag{8}$$

The system (1)–(7) is solved using the three-dimensional contact SPH method[31] where a continuous material is represented by a set of SPH particles $i = 1, \ldots, N$ with masses m_i and sizes $D_i = (m_i/\rho_i)^{1/3}$. Two neighbor particles i and j separated by the distance $|\mathbf{r}_i - \mathbf{r}_j|$ interact via a smoothing kernel W_{ij} allocated within a smoothing distance $h_{ij} = \alpha(D_i + D_j)$. The interaction between i and j particles depends on their relative velocity, the equation of states of particle materials, and the used type of smoothing kernel $W_{ij}(|\mathbf{r}_i - \mathbf{r}_j|/h_{ij})$.

The particle interaction scheme implemented in our in-house cSPH code is shown in Fig. 1. The superscript "*" denotes a solution of the 1D Riemann problem along the axis R connecting a pair of interacting SPH particles. A solution for the transversal discontinuity problem is obtained using the acoustic approximation,[31] while the longitudinal discontinuity problem can be solved using both the acoustic approximation and the non-iterative method[32] utilizing parameters of the shock Hugoniot.

Equations (1)–(3) can be rewritten in cSPH form using the Riemann problem solution at interparticle contacts.[31] Strains in particles are calculated from the velocity field
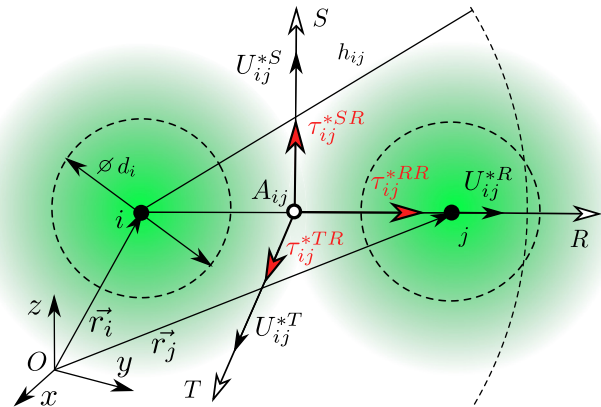

FIG. 1. SPH-particle interaction scheme. Discontinuity is placed along the R-axis which passes through the centers of interacting particles i and j. The R-axis is perpendicular to the contact surface ST at the middle point A_{ij} between the particles. Components of the stress τ_{ij}^* at the contact surface are provided by a Riemann solver. The results of the interaction are the longitudinal waves of compression/rarefaction propagating from the contact surface ST along the R-axis into i and j particles and the two transversal shear waves propagating across the perpendicular planes RS and RT.

during the solution of the system (1)–(8). The volumetric strain rate $\dot{\theta} = \dot{\varepsilon}^{xx} + \dot{\varepsilon}^{yy} + \dot{\varepsilon}^{zz}$ derived from Eq. (1) is given by

$$\frac{d\theta_i}{dt} = \dot{\theta}_i = 2\sum_j \frac{m_j}{\rho_j}\left[\left(U_{ij}^{R*} - U_i^R\right)\mathbf{e}^R\right]\cdot\nabla_i W_{ij}. \quad (9)$$

Momentum conservation (2) in cSPH form is

$$\frac{d\mathbf{U}_i}{dt} = -2\sum_j \frac{m_j\left(P_{ij}^* l^{R\alpha} - S_{ij}^{\gamma R*} l^{\gamma\alpha}\right)}{\rho_j \rho_i}\nabla_i W_{ij}. \quad (10)$$

Energy conservation (3) in cSPH form is

$$\frac{dE_i}{dt} = -2\sum_j \frac{m_j\left(P_{ij}^* U_{ij}^{R*} - S_{ij}^{\gamma R*} U_{ij}^{\gamma*}\right)\mathbf{e}^R}{\rho_j \rho_i}\cdot\nabla_i W_{ij}. \quad (11)$$

Here, $\mathbf{e}^R = (\mathbf{r}_j - \mathbf{r}_i)/(|\mathbf{r}_j - \mathbf{r}_i|)$ is the i to j direction vector, $l^{R\alpha} = (x_j^\alpha - x_i^\alpha)/(|\mathbf{r}_j - \mathbf{r}_i|)$ is the direction cosine, $\gamma = R, S, T$, and $\alpha = x, y, z$.

Then, the density evolution is expressed precisely using the strain rate (9)

$$\rho_i^{n+1} = \rho_i^n \exp\left(-\dot{\theta}_i \Delta t\right), \quad (12)$$

where Δt is the integration time step between the time layers n and $n+1$. The cSPH-forms of the strain rate tensor (7) and the stress deviator tensor (5) were presented in detail earlier.[31]

The SPH particle representation of a continuous material allows us to deal naturally with the formation of discontinuities such as voids and cracks produced by the strong enough tensile stress. Stress-strain evolution of the material in each particle can be easily tracked during modeling. The failure process is supposed to be local and develops independently in each particle. The plastic strain, ε_p, which is assumed to correspond to a partially damaged state of a material having some current strength, is given by the difference between the total strain ε provided by the strain rate equation (9) and the elastic strain ε_e

$$\varepsilon_p = \varepsilon - \varepsilon_e. \quad (13)$$

Failure transformation of ceramics is accompanied by the elastic to internal energy transfer which should be included in the equation of state (8) as a correction term in pressure.[29] During the failure, the material strength decreases, and the elastic stress deviator **S** obtained in (5) should be corrected at each simulation step. The following failure model provides the required adjustment.

III. AN EXPLICIT FAILURE MODEL FOR CERAMICS

A. Model description

The basic JH-1,[26] JH-2,[27] and JHB[28] models, ideas of which are developed in this paper, assume the intact material to have the strength $\sigma_i(P)$ depending on pressure (see Fig. 2). Then, the uniaxial loading can only deform the material
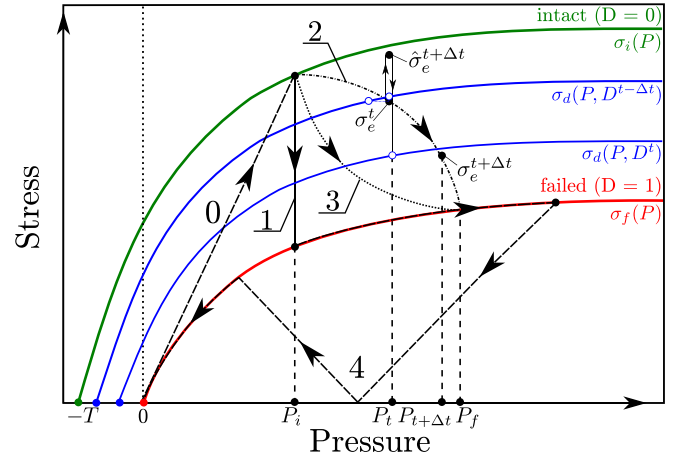

FIG. 2. The typical scheme for a boron carbide failure process on a diagram "equivalent stress-pressure" in plate-impact experiments. The failure process begins in an element of material elastically loaded along path 0 if its equivalent stress $\sigma_e \geq \sigma_i(P)$. Then, there are several ways to proceed to a failed state. Path 1 used in JH-1 and JHB models corresponds to the instantaneous failure, at which the plastic strain increment $\Delta\varepsilon_p^i$ is calculated via (20). Path 2 used in the JH-2 model corresponds to the gradual failure (22) with the acceleration of the damage rate. The equivalent stresses at steps t and $t + \Delta t$ are shown on this path to illustrate our non-iterative algorithm of the gradual damage. Path 3 (this work) corresponds to a solution of the kinetic equation (27) with a decelerating damage rate in the approach to the completely failed state with $\sigma_e = \sigma_f(P)$. Path 4 shows the uniaxial unloading of a completely damaged material, in which $\sigma_e \leq \sigma_f(P)$ for all states.

elastically to states lying below this limiting function. If the equivalent stress σ_e exceeds this limit, the failure process begins, resulting in strength reduction to a lower strength limit $\sigma_d < \sigma_i(P)$ in a partly damaged state of the material. On the other hand, the strength of the completely failed material is limited by a function $\sigma_f(P)$ as shown in Fig. 2. Although the physical mechanisms of ceramics failure are not well understood, its kinetics can be postulated by using the mechanical properties and empirically defined characteristics only; among these, the unknown function $\sigma_f(P)$ is adjusted in an attempt to reproduce the experimental results in simulations.

The material stress state is characterized by the stress deviator tensor $S^{\alpha\beta}$ using which an equivalent stress can be defined as $\sigma_e = \sqrt{3J_2}$

$$\sigma_e^2 = \frac{3}{2}S^{\alpha\beta}S^{\beta\alpha} = \frac{1}{2}\{(S^{xx} - S^{yy})^2 + (S^{yy} - S^{zz})^2$$
$$+ (S^{xx} - S^{zz})^2 + 6[(S^{xy})^2 + (S^{xz})^2 + (S^{yz})^2]\}, \quad (14)$$

where J_2 is the second stress tensor invariant and subscripts $\alpha = x, y, z$, $\beta = x, y, z$.

The actual strength σ_d varies throughout the failure process between the intact $\sigma_i(P)$ and the completely failed material strength $\sigma_f(P)$ and depends on a dimensionless damage parameter $D \in [0, 1]$ via a simple linear relationship[29]

$$\sigma_d(P, D) = \sigma_i(P) - D(\sigma_i(P) - \sigma_f(P)). \quad (15)$$

The damage parameter is assumed to determine a damage degree of the material uniquely, and its increment ΔD at each simulation step Δt is consistent with the corresponding plastic strain increment $\Delta\varepsilon_p$.[29] The last is defined as a

difference between the total strain $\Delta\varepsilon$ calculated from the continuity equation (1) and the elastic strain $\Delta\varepsilon_e$

$$\Delta\varepsilon_p = \Delta\hat{\varepsilon} - \Delta\varepsilon_e. \tag{16}$$

The damage parameter in the JH-2 and JHB models is defined similarly to the Johnson–Cook approach[33]

$$D = \sum \Delta D = \sum \frac{\Delta\varepsilon_p}{\varepsilon_p^f}, \tag{17}$$

where ε_p^f is a total plastic strain accumulated in a transition from the intact to the completely failed material in a given element. This intuitive definition of D needs a clarification on how to evaluate both the plastic strain increment $\Delta\varepsilon_p$ and ε_p^f.

To estimate a plastic strain increment at each simulation step, we suggest to use the expression[34]

$$\Delta\varepsilon_p = \frac{\hat{\sigma}_e - \sigma_e}{3G}, \tag{18}$$

where G is a shear modulus and $\hat{\sigma}_e$ is an equivalent stress obtained via Eq. (1) assuming that the total strain increment is entirely elastic, that is, $\Delta\varepsilon_p = 0$ in (16). The stress deviator tensor (5) calculated with that assumption is denoted as $\hat{S}^{\alpha\beta}$. The magnitude of $\hat{\sigma}_e$ is then calculated using (14). If $\hat{\sigma}_e > \sigma_d$, then the stress deviator is corrected using the von Mises yield criterion

$$S^{\alpha\beta} = \frac{\sigma_d}{\hat{\sigma}_e}\hat{S}^{\alpha\beta}, \quad \sigma_e = \sigma_d. \tag{19}$$

Using Eq. (18), one may find that the plastic strain increment $\Delta\varepsilon_p^i$ in a sudden transition from an intact to failure state at a fixed pressure P_i, as it is illustrated by vertical line 1 in Fig. 2, is

$$\Delta\varepsilon_p^i(P_i) = \frac{\sigma_i(P_i) - \sigma_f(P_i)}{3G}. \tag{20}$$

After that, the material should be considered as completely failed with $D = 1$ which gives

$$\varepsilon_p^f = \Delta\varepsilon_p^i(P). \tag{21}$$

During a gradual failure process, one has to solve the kinetic equation

$$\frac{dD}{dt} = \frac{1}{\varepsilon_p^f}\frac{d\varepsilon_p}{dt}, \tag{22}$$

where the expression for ε_p^f is unknown.[35] However, with failure transitions shown in Fig. 2 and using (18), its magnitude can be written as follows:

$$\varepsilon_p^f = \varepsilon_p^f(P_i, P_f) = \int_{P_i}^{P_f} d\varepsilon_p. \tag{23}$$

As soon as P_i and P_f are defined by loading conditions, this expression varies depending on a path of failure transition on the σ–P plane plotted in Fig. 2. Therefore, it cannot be exactly evaluated until the failure process completes.

The unknown ε_p^f can be approximated by a function $\varepsilon_p^f(P)$ which depends only on pressure during failure transition. However, the problem is to find the best function to satisfy the condition

$$1 = \int_{P_i}^{P_f} dD = \frac{1}{\varepsilon_p^f}\int_{P_i}^{P_f} d\varepsilon_p \simeq \int_{P_i}^{P_f} \frac{d\varepsilon_p}{\varepsilon_p^f(P)}, \tag{24}$$

for *any* path of failure transition. Johnson and Holmquist[27,29] proposed the following function:

$$\varepsilon_p^f(P) = D_1\left(\frac{P+T}{P_{\text{HEL}}}\right)^{D_2}, \tag{25}$$

with the fitting parameters D_1 and D_2. Using a set of particular experiments, one may find a reasonable fit. Thus, the above fitting function $\varepsilon_p^f(P)$ with two additional parameters supplements the JH failure model. Those parameters are related to other material characteristics used in the failure model. Below, we demonstrate that such a fitting approach is unnecessary, and a simpler form of function $\varepsilon_p^f(P)$ depending on already defined characteristics can be utilized.

By considering a loading path with a quite small difference between P_i and P_f, the best choice for ε_p^f should be close to the plastic strain increment at sudden failure $\Delta\varepsilon_p^i$ (20). Thus, for the proposed model, we suggest the best $\varepsilon_p^f(P)$ to be

$$\varepsilon_p^f(P) = \Delta\varepsilon_p^i(P) = \frac{\sigma_i(P) - \sigma_f(P)}{3G}. \tag{26}$$

The advantage of this simple definition is that it does not introduce the additional fitting parameters into our failure model yet provides the same or even better simulation accuracy as we show in Sec. IV B.

One should notice that calculations with the expression (17) lead to acceleration of the failure process with an approach to the completely damaged material $D = 1$ along curve 2 in Fig. 2. The code must reset the parameter D to unity if it exceeds 1. To remedy this, the proposed damage rate equation (22) is multiplied by the factor $(1 - D)$

$$\frac{dD}{dt} = (1 - D)\frac{1}{\varepsilon_p^f(P)}\frac{d\varepsilon_p}{dt}. \tag{27}$$

It results in a smooth deceleration at the final stage of the failure process which is illustrated by curve 3 in Fig. 2. The damage parameter D may only asymptotically approaches to unity so that the complete failure with $D = 1$ cannot be reached for a finite span of loading. Our simulations demonstrate that the most damaged material is typically characterized by the damage parameters with $D \leq 0.999$. This result will be shown to be consistent with the experimental data.

The finite difference integration of (27) can be performed as follows: Considering magnitudes of $d\varepsilon_p/dt$ and ε_p^f to be constant during a simulation step from t to $t + \Delta t$, we have

$$\ln\frac{1 - D^{t+\Delta t}}{1 - D^t} = -\frac{\Delta\varepsilon_p}{\varepsilon_p^f}, \tag{28}$$

which finally results in

$$D^{t+\Delta t} = 1 - (1 - D^t) \exp\left(-\frac{\Delta \varepsilon_p}{\varepsilon_p^f}\right). \qquad (29)$$

Here, the intact and failure stress dependencies on pressure are used in the form introduced for the JHB model.[28] The function for $\sigma_\lambda(P)$ is given by

$$\begin{cases} \sigma_\lambda(P) = \sigma_\lambda^0 + (\sigma^{\max_\lambda} - \sigma_\lambda^0) \\ \qquad \times \{1 - \exp\left[-\alpha_\lambda(P - P_\lambda^0)\right]\}, \quad P > P_\lambda^0, \\ \sigma_\lambda(P) = \sigma_\lambda^0(P + T_\lambda)/(P_\lambda^0 + T_\lambda), \quad P < P_\lambda^0, \end{cases} \quad (30)$$

with

$$\alpha_\lambda = \sigma_\lambda^0 / \left[(\sigma^{\max_\lambda} - \sigma_\lambda^0)(P_\lambda^0 + T_\lambda) \right], \qquad (31)$$

where $\lambda = i, f$ is either for the intact or for the failed material.

The tensile strength T was also supposed[29] to be linearly dependent on the damage parameter D as $T_i = T_0(1 - D)$. The parameters σ_λ^0, $\sigma^{\max_\lambda}$, P_λ^0 are fitted to provide the best agreement between simulations and experiments. The strength limit dependency on the strain rate should also be taken into account.[3] Following the previous works,[29,33] we use

$$\sigma_\lambda(P, \dot{\varepsilon}^*) = \sigma_\lambda(P)(1.0 + C \ln \dot{\varepsilon}^*), \qquad (32)$$

where $\dot{\varepsilon}^* = \dot{\varepsilon}_e / \dot{\varepsilon}_0$ is the dimensionless strain rate with $\dot{\varepsilon}_0 = 1.0 \, \text{s}^{-1}$ and C is the constant. The equivalent strain rate can be found from the expression

$$\dot{\varepsilon}_e^2 = \frac{2}{9} \left[(\dot{\varepsilon}^{xx} - \dot{\varepsilon}^{yy})^2 + (\dot{\varepsilon}^{yy} - \dot{\varepsilon}^{zz})^2 + (\dot{\varepsilon}^{xx} - \dot{\varepsilon}^{zz})^2 \right] \\ + \frac{1}{3} \left[(\dot{\gamma}^{xy})^2 + (\dot{\gamma}^{yz})^2 + (\dot{\gamma}^{xz})^2 \right], \qquad (33)$$

where $\gamma^{\alpha\beta} = 2\varepsilon^{\alpha\beta}$.

Non-hydrostatic compression leading to the localized damage process associated with amorphization on an atomic scale[13–15] may produce amorphous ceramics of different densities.[24] The consistent model should take into account a local transition from a crystal to an amorphous phase, but its equation of state is unknown. To take into account the elastic energy conversion to internal energy in the failure process, the JH-2 model[27,29] was proposed to add a positive pressure surplus ΔP for the damaged material, which reduces the equilibrium density of amorphous ceramics. The pressure surplus can be estimated by accounting the elastic energy ΔK dissipation induced by the strength loss (see Fig. 2)

$$\Delta K^t = \frac{\sigma_d^2(P^t, D^{t-\Delta t})}{6G} - \frac{\sigma_d^2(P^t, D^t)}{6G}, \qquad (34)$$

$$\Delta P^{t+\Delta t} = -B\mu^{t+\Delta t} + \sqrt{(B\mu^{t+\Delta t} + \Delta P^t)^2 + 2\beta B \Delta K^t}, \quad (35)$$

where B is the bulk modulus, $\mu = \rho/\rho_0 - 1$, and $\beta \in [0, 1]$ is a fitted bulking factor. Equation (35) can be applied only at compression with $\mu > 0$.[29]

B. Equation of state

Volumetric compression of boron carbide in DAC experiments[16] does not demonstrate phase transitions up to 70 GPa. According to these results, we do not include phase transitions to the model in contrast to the JHB.[30] For the reference pressure curve (Fig. 3) in the boron carbide's equation of state, we use the experimental data fit in the form of the Murnaghan equation

$$P_r(\rho) = \frac{\rho_0 c_0^2}{n} \left[\left(\frac{\rho}{\rho_0} \right)^n - 1 \right], \qquad (36)$$

where ρ_0 is the normal density, c_0 is the bulk sound speed, and n is the power parameter. The pressure is calculated according to the Mie–Gruneisen equation of state

$$P = P_r + \Gamma \rho (e - e_r) + \Delta P, \qquad (37)$$

where Γ is the Gruneisen parameter, e_r is the reference specific energy obtained by integration of Eq. (36)

$$e_r(\rho) = \frac{c_0^2}{n} \left[\frac{\rho_0}{\rho} - 1 + \frac{(\rho/\rho_0)^{n-1} - 1}{n-1} \right], \qquad (38)$$

ΔP is the pressure surplus (35) which is found to fit well the experimental wave profiles. All material characteristics including the fitting parameters of the failure model used in simulations are listed in Table I.

C. Numerical algorithm

Before we proceed to the ceramic failure algorithm, the solutions of Eqs. (1)–(3), namely, $\rho^{t+\Delta t}$, $\mathbf{U}^{t+\Delta t}$, $e^{t+\Delta t}$, and $\dot{\varepsilon}^{\alpha\beta}$, are supposed to be found for each SPH-particle. CFD simulations are performed using the first order accuracy scheme, and the local strain rate $(\dot{\varepsilon}^{\alpha\beta})^t$ remains constant during the time step Δt.

The step-by-step non-iterative algorithm is given below for a single SPH-particle in which the local failure process takes place.
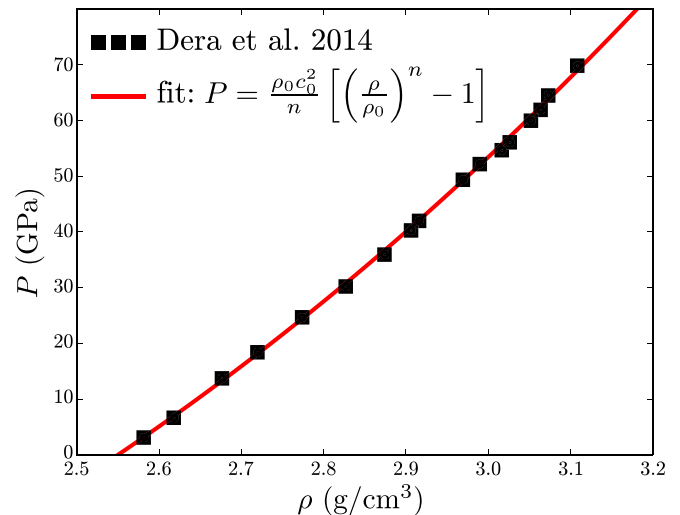

FIG. 3. Reference pressure (36) fitted for B$_4$C using DAC experiment[16] data.

TABLE I. B$_4$C parameters used in simulations of experiments by Vogler *et al.*[9] (to the left of ||) and by Grady *et al.*[8] (to the right of ||).

Material characteristics	Value
Initial density ρ_0, kg/m^3	2550
Volumetric sound velocity c_0, km/s	10
Equation of state exponent n	3
Bulk modulus B, GPa	255
Shear modulus G, GPa	216
Gruneisen parameter Γ	0.8
HEL strength σ_{HEL}, GPa	14.0
HEL pressure P_{HEL}, GPa	8.8
Intact strength constant σ_i^0, GPa	6.7
Intact strength constant $\sigma_i^{\max}$, GPa	14.3
Intact strength constant P_i^0, GPa	2.3
Failure strength constant σ_f^0, GPa	5.0 || 1.
Failure strength constant $\sigma_f^{\max}$, GPa	8.5 || 2.
Failure strength constant P_f^0, GPa	5.0 || 2.
Hydrostatic tensile strength T, GPa	0.27
Strain rate constant C	0.01
Bulking factor β	1.0

Step 1: By the moment $t + \Delta t$, the stress tensor increment (5) is calculated assuming all strains in Δt to be elastic, i.e., without accounting damage in ceramics

$$(\hat{S}^{\alpha\beta})^{t+\Delta t} = (S^{\alpha\beta})^t + 2G(\dot{\varepsilon}^{\alpha\beta})^t \Delta t.$$

After that, the stress tensor rotation (5) is also performed.
Step 2: Using dependency (14), the equivalent stress $\hat{\sigma}_e^{t+\Delta t}$ is calculated using the updated stress deviator tensor $(\hat{S}^{\alpha\beta})^{t+\Delta t}$.
Step 3: The equivalent strain rate $\dot{\varepsilon}_e^t$ is calculated using (33).
Step 4: New strength limit is calculated according to the current damage parameter

$$\sigma_d^{t+\Delta t} = \sigma_i^t - D^t(\sigma_i^t - \sigma_f^t).$$

Step 5: If $\hat{\sigma}_e^{t+\Delta t} > \sigma_d^{t+\Delta t}$, the correction (19) is applied.
Step 6: If $\mu = \rho^{t+\Delta t}/\rho_0 - 1 > 0$, the pressure surplus is calculated as follows:

$$\Delta P^{t+\Delta t} = -B\mu + \sqrt{(B\mu + \Delta P^t)^2 + 2\beta B \Delta K^t},$$

else keep the current value of ΔP

$$\Delta P^{t+\Delta t} = \Delta P^t. \tag{39}$$

Step 7: Obtain $P^{t+\Delta t}$ using the expression (37).
Step 8: Define the intact and the failed strength limits

$$\sigma_\lambda^{t+\Delta t} = \sigma_\lambda(P^{t+\Delta t}, (\dot{\varepsilon}^*)^t), \quad \lambda = i, f$$

using the expressions (30) and (31).
Step 9: If the failure process takes place, $\Delta\varepsilon_p$ and ε_p^f are calculated as follows:

$$\Delta\varepsilon_p^t = \frac{\hat{\sigma}_e^t - \sigma_e^t}{3G}, \quad (\varepsilon_p^f)^t = \frac{\sigma_i^t - \sigma_f^t}{3G},$$

else proceed to step 12.

Step 10: Update the damage parameter

$$D^{t+\Delta t} = 1 - (1 - D^t) \exp\left(-\frac{\Delta\varepsilon_p^t}{(\varepsilon_p^f)^t}\right).$$

Step 11: The damage induced change in the elastic energy at one simulation step

$$\Delta K^{t+\Delta t} = \frac{\sigma_d^2(P^{t+\Delta t}, D^t)}{6G} - \frac{\sigma_d^2(P^{t+\Delta t}, D^{t+\Delta t})}{6G}.$$

Step 12: Proceed to a next time step of integration of motion equations (1)–(3).

The proposed non-iterative algorithm given above is a part of the contact SPH method in which the strain rate $\dot{\varepsilon}_{\alpha\beta}$ is calculated by using the velocity at the inter-particle contact obtained from a solution of the Riemann problem. This strain rate remains constant during the time step Δt. Other methods with a higher order time accuracy may have a variable $\dot{\varepsilon}_{\alpha\beta}$ during Δt, but this failure algorithm is only tested with the cSPH method.

IV. FITTING AND VALIDATION OF THE FAILURE MODEL

A. Simulation setup

As in the original works,[29,30] the fitting of model parameters is performed with using the available experimental wave profiles. Here, to fit the material characteristics and damage model parameters, we use the target/LiF interface velocities measured by Vogler *et al.*[9] in plate-impact experiments with the VISAR technique. Then, the fitted model parameters are put to the test with the help of the interface velocities obtained by Grady *et al.*[8] in similar experiments but with a different kind of B$_4$C ceramic. The failure process may vary due to the manufacturing standard, and, as demonstrated below, the developed failure model is applicable for different samples if the mere strength of a failed material is properly adjusted.

Simulations of shock waves generated by plate impacts are performed using our in-house 3D cSPH code.[36,37] The 1D-like shock propagation along the *x*-axis is simulated in conditions similar to the aforementioned experimental sets. Impactors made up of different materials were used in the experiments, and the same materials are simulated with the corresponding equation of states.[7]

Each sample is represented by a material layer placed along the *x*-axis with a thickness chosen according to a particular experiment. The number of SPH-particles for this direction is of an order 10^3, and those particles have the diameter $d_i \sim 0.7\,\mu$m, which determines a spatial resolution in our simulations. Typically, 15 particles are set along *y* and *z* directions of the layer with the cross-section $100 \times 100\,\mu$m^2. SPH particles are arranged by a random close packing into a liquid-like structure that excludes numerical effects of a lattice packing. Periodical boundary conditions are imposed along *y* and *z* axes. The thickness for a LiF-window is chosen in such a way that a rarefaction wave from its free surface does not interfere with a wave passing through a target/window interface. The

velocity of a target/window interface $u_a(t)$ is taken from a set of target's particles adjacent to window's particles, and then, it is compared with an experimental velocity profile $u_a(t)$.

The examples of spatial 2D distribution and 1D profiles of the averaged damage parameter and mass velocity obtained from such plate-impact simulation of a wider sample with the cross-section of $3200 \times 100 \ \mu m^2$ represented by 480×15 SPH particles along y and z directions are shown in Fig. 4. An impactor and a target are made up of the same boron carbide. The impactor with a backer (or without it) is directed to the target with the velocity of 2076 m/s.

The impactor-target interaction results in shock wave formation which propagates toward a target/window interface with the velocity profile $u(x)$ shown in the lower half of Fig. 4. Such a spatial profile of mass velocity cannot be observed directly in experiments. However, failure processes inside a sample are embodied in the target/window interface velocity $u_a(t)$ which can be measured with a reasonable time resolution. The characteristic features of the interface velocity profile are originated from four distinct regions of the spatial velocity profile $u(x, t)$ arriving at the interface. Those regions can be altered by adjusting the corresponding model parameters.

Figure 4 shows wave profiles just after the arrival of the elastic precursor wave to the interface. As a result of the wave interaction with the LiF window, the reflected rarefaction wave and transmitted elastic shock wave are formed (see the corresponding arrows in Fig. 4). The a–b region corresponds to an undisturbed part of the initial elastic precursor, where the mass velocity profile $u(x)$ is determined by the intact strength σ_i which is close to σ_{HEL}.

The b–c region corresponds to a transition from purely elastic to plastic deformation where the failure process occurs gradually. It results in the formation of a damage front b–c with increasing pressure and decreasing equivalent stress along path 3, as shown in Fig. 2. The front structure is governed by the failure rate equation (22).

The height of plateau c–d just behind the plastic wave front depends on the impact velocity and the equation of state (37). Its length is determined by a distance propagated by a rarefaction wave for a given span of time. This unloading wave starts from the left free boundary of the impactor and propagates toward the failure front in a partially failed material. It results in the formation of the d–e region on the velocity profile, whose structure is determined by a spatial distribution of the remanent strength $\sigma_d(x)$ in the partially damaged target and impactor.

All spatial features of mass velocity profiles $u(x, t)$ arriving at the interface produce the corresponding time domains in the interface velocity $u_a(t)$. Comparing the experimental and calculated $u_a(t)$, we can adjust the corresponding model parameters with the aim to reproduce the aforementioned characteristics of experimental wave profiles.

B. Fitting the model to profiles obtained by Vogler *et al.*

We adjust all model parameters listed in Table I, excluding those related to the used equation of state, to reproduce in simulation the main features of experimental interface velocity profiles including the heights of the elastic precursor and plastic wave, the delay between arrivals of these two waves, the rise time of the damage front, the plastic plateau duration, and the decline rate of velocity after arrival of the unloading wave.

The interface velocity profiles obtained by Vogler *et al.* in experimental tests[9] are divided into three groups as follows:

1. Constant-shock BC-I–BC-V with a wide plateau behind the shock front [the thick 8 mm target of boron carbide and metallic Ta/Cu impactor, Fig. 5(a)];
2. Shock-release BC-VI–BC-XI with the rarefaction velocity history [the boron carbide impactor with the light TPX backer, Fig. 5(b)];
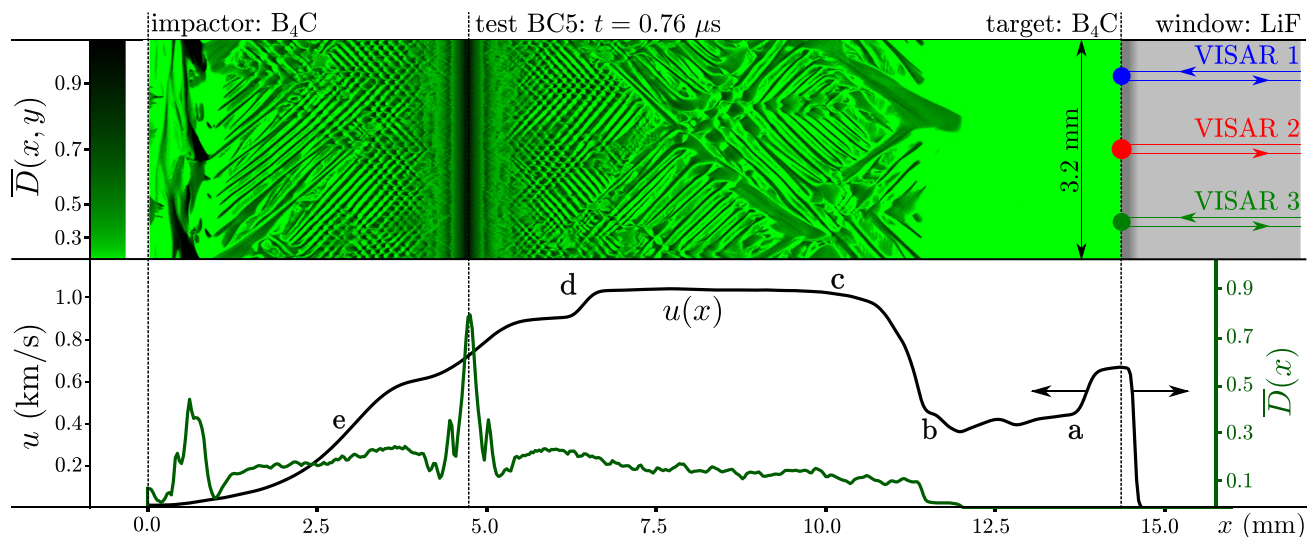

FIG. 4. Map of averaged damage parameter $\bar{D}(x, y)$ on the top with the corresponding averaged profiles of flow velocity and damage parameter $\bar{D}(x)$ after the arrival of the shock wave to the target/window interface. The impact velocity is 2076 m/s. The almost completely damaged material with $\bar{D} \approx 1$ is formed only in the vicinity of the contact between the impactor and the target. Two families of failure bands are generated within the damage front c–d with shock propagation. The interface velocities picked up in three points are presented in the Movie). About 40×10^6 SPH particles are involved in the simulation. Multimedia view: https://doi.org/10.1063/1.5043418.1
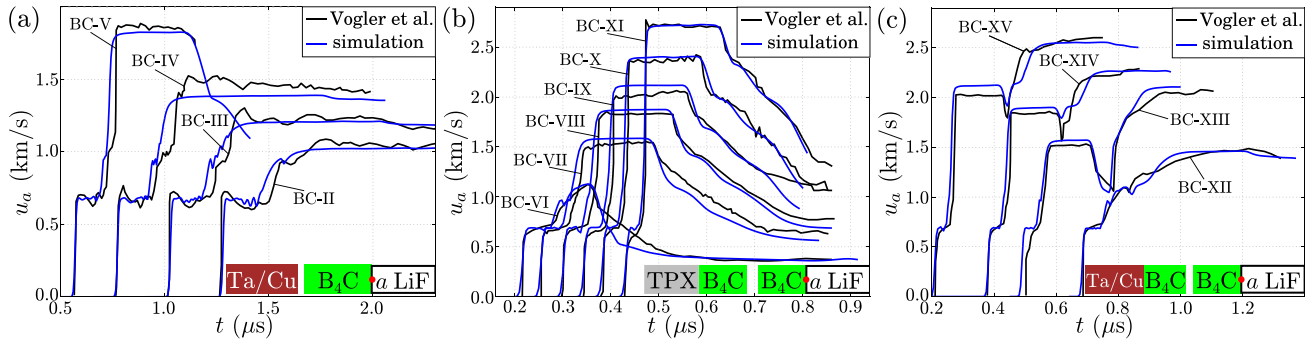
FIG. 5. Simulated (blue curves) and experimental (black curves) interface velocities $u_a(t)$ as functions of time for the tests conducted by Vogler et al.:[9] (a) constant-shock BC-II–BC-V with a thick B_4C target and Ta or Cu impactors; (b) shock-release BC-VI–BC-XI with a B_4C target and an impactor backed with a light TPX material; and (c) shock-reshock BC-XII–BC-XV with a B_4C target and an impactor backed with a heavy metallic material. The target/LiF window interfaces are marked by "a." The used model parameters listed in Table I were adjusted to reproduce the main features of the experimental velocity $u_a(t)$.

3. Shock-reshock BC-XII–BC-XV with the additional load from the Ta/Cu backer behind the boron carbide impactor presented in Fig. 5(c).

The simulated interface velocities shown in Figs. 5(a)–5(c) fit the different experimental groups with reasonable accuracy. Transitions from the elastic precursor to the plastic wave are reproduced well in all three groups.

As it is noted earlier, the rarefaction wave profile depends much on the strength of the failed material $\sigma_f(P)$ which is shown in Fig. 6. Therefore, the simulated amplitude of the elastic release is slightly lower than the experimental one for the tests BC-VI and BC-VII in the second group, but it agrees well with the other tests BC-VIII–BC-XI for higher impact velocities. One may obtain even better agreement for the whole group by varying a low-pressure part of the $\sigma_f(P)$ curve.[30]

The interface velocities in the third group [BC-XII–BC-XV, Fig. 5(c)] also have some peculiar features. A thin low-dense glue junction with the thickness of several μm between an impactor and a heavy backer was introduced[30] to provide the additional release at the impactor/backer interface before
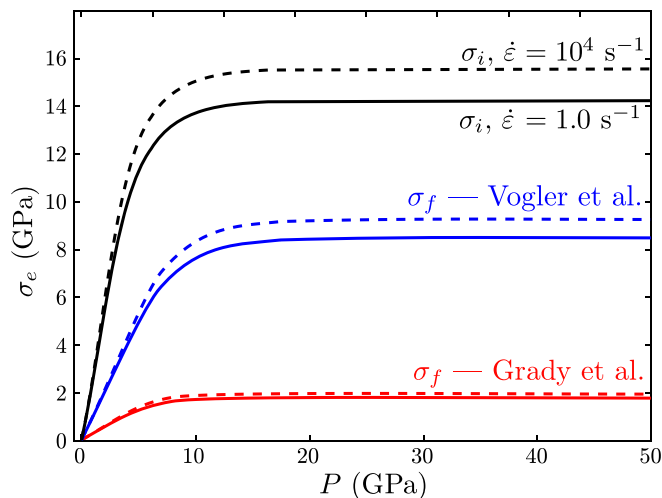

FIG. 6. The pressure dependencies of intact $\sigma_i(P)$ and failed strength $\sigma_f(P)$ fitted for the best agreement with two sets of experimental data. Solid curves show the strength at a relatively low strain rate $\dot{\varepsilon} = 1\,\text{s}^{-1}$, while the dashed curves correspond to a higher strain rate $\dot{\varepsilon} = 10^4\,\text{s}^{-1}$. The corresponding failure parameters are listed in Table I.
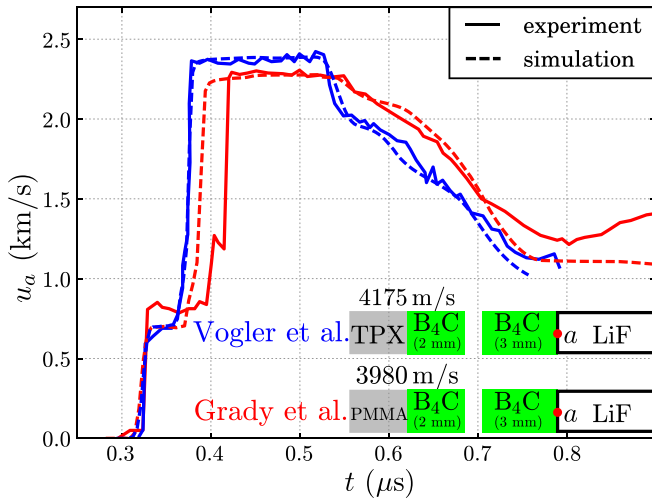
reshock. To simulate such a behavior, the small gap of $10\,\mu m$ is placed between the impactor and the backer. The larger gap should be taken for the BC-XIII test ($60\,\mu m$). This could be a result of the backer/impactor detaching during acceleration, which leads to an additional time lag of the reshock.[9]

C. Validation of the model by profiles obtained by Grady et al.

The model parameters fitted to the experimental data by Vogler et al.[9] and listed in Table I are then used for simulation of another set of experimental interface velocities obtained by Grady et al.[8] We found that the damage transition from the elastic to the plastic wave is reproduced poorly, most likely because the boron carbide samples used in Ref. 8 were made using a manufacturing process differed from that in Ref. 9. Since the material strength of boron carbide may vary, it is worthwhile to adjust it for the given samples in the damage model. It was found that the strength function $\sigma_f(P)$ of the completely failed material can be varied solely to take into account this effect.

Before we proceed to the simulation results, one should pay attention to the BC10[8] test which is almost identical to BC-X.[9] The velocity histories for these tests are shown in Fig. 7. Despite the similar initial setup, the waves look rather different from what was indicated earlier.[30] A natural reason for that could be in different manufacturing technologies used in these experimental sets. In the BC10[8] test, the elastic precursor is longer, but the elastic release is shorter than one in the BC-X test.[9]

To describe such a difference, we reduced σ_f by several times (but keep the same σ_i and other model parameters) as shown in Fig. 6. It was enough to obtain a good agreement with the experimental velocities.[8] Such adjustment not only results in the smaller elastic release amplitude but also slows down the failure process (27) due to an increase in $\varepsilon_p^f(P)$ introduced in our damage model by (26). The duration of the elastic precursor also grows, which agrees well with the experimental profiles.

Figure 8 shows other tests conducted by Grady et al. The lower $\sigma_f(P)$ presented by the red curve in Fig. 6

FIG. 7. Simulated and experimental interface velocities for two datasets obtained in similar experiments[8,9] but using different kinds of boron carbide. The different failed strengths shown in Fig. 6 are required to match the simulated velocities with the experimental ones.

them increase with shock propagation, but the damage degree $\bar{D}(x)$ averaged across the sample remains near 16% as seen in Fig. 4. Such broadening of the failure bands is associated with the increase in the damage front thickness, which can be observed in the Movie (Multimedia view). The damage front has the near zero thickness just after the impact, which produces sudden failure of all SPH particles near the contact. With the increase in the front thickness, the corresponding damage rate decreases, resulting in a more gradual failure process, which makes possible the local shear stress relaxation around a failure element of the material. Propagation of such stress relaxation from the growing failure bands prevents damaging between the bands.

The arrival of the damage front with the grid of failure bands to the interface causes slightly different interface velocities picked up in different locations by VISAR beams. Such a phenomenon realized in our simulation [see Fig. 4 and Movie (Multimedia view)] was also experimentally observed.[9]

V. CONCLUSION

The new explicit failure model for ceramics is developed on the basis of the previous approaches proposed by Johnson and Holmquist. The new damage rate equation with the simplified total plastic strain in the completely damaged material can be solved explicitly at each simulation step. The model is implemented in our in-house cSPH code through the use of the non-iterative algorithm.

The failure model is successfully fitted and validated by SPH simulation of the interface velocity profiles obtained in plate-impact experiments with two different kinds of boron carbide. The model provides a good agreement with all features observed in the experimental profiles, including the leading elastic precursor followed by the plastic/failure front and the velocity plateau followed by the release wave.

We found that the material strength of the failed boron carbide must be adjusted to ensure the applicability of the failure model to various samples of boron carbide manufactured differently. This suggests that a unique relationship between the shear strength of failed ceramic and its inner structure may exist.

The developed failure model is applicable for many ceramic materials exhibiting strength reduction under heavy
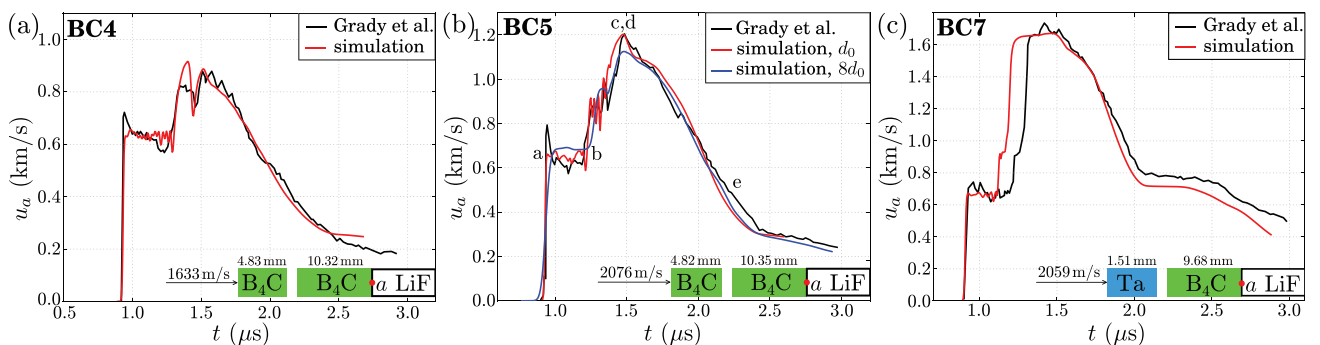
provides the excellent agreement between the simulated and experimental interface velocities.

We used a similar spatial resolution of all simulated samples with the numbers of particles about $x \times y \times z \approx 10^3 \times 15 \times 15$ with one exception shown in Fig. 4. To check whether the spatial resolution affects the obtained results, the test BC5 is simulated with the increased particle size (2, 4, and 8 times as much). It is clearly seen in Fig. 8(b) that the main features of the velocity profile remain. Thus, simulation with larger SPH particles does not induce noticeable errors, excepting some smoothing of the damage front.

To demonstrate how the spatial distribution of the damage degree is formed inside the material after shock propagation, the large-scale simulation of the BC5[8] experiment is performed. The lateral dimension of the sample along the y-axis is extended up to 3.2 μm.

Figure 4 demonstrates that the failure bands of the heavily damaged material are generated within the damage front between the elastic precursor and the plastic wave. Those bands grow along the maximal shear stress direction at the angles of $\pm 45°$ to the direction of shock propagation, which results in a failure grid consisting of two band families. Both the thickness of bands and the distance between

FIG. 8. Simulated and experimental interface velocities for the BC4, BC5, and BC7 tests.[8] The target/LiF window interfaces are marked by "*a*." Frame (b) shows an extra blue-colored profile from simulation using SPH particles with diameters increased by factor 8. In contrast to simulations shown in Fig. 5, here the only material strength $\sigma_f(P)$ was adjusted to reproduce the experimental velocities (see also Figs. 6 and 7).

stress, such as silicon carbide SiC and aluminum nitride AlN. Thus, the model embedded in the computational codes can describe specific ceramics by adjusting the failure parameters but without revision of the model itself.

ACKNOWLEDGMENTS

[1]F. Thévenot, J. Eur. Ceram. Soc. **6**, 205 (1990).
[2]D. E. Grady, J. Appl. Phys. **117**, 165904 (2015).
[3]D. E. Grady, Mech. Mater. **29**, 181 (1998).
[4]M. L. Wilkins, "Third progress report of light armor programm," Technical Report No. UCRL50460, Lawrence Livermore National Laboratory, University of California, CA, 1968.
[5]W. H. Gust and E. B. Royce, J. Appl. Phys. **42**, 276 (1971).
[6]M. N. Pavlovskii, Sov. Phys. Solid State **12**, 1736 (1971).
[7]*LASL Shock Hugoniot Data*, edited by S. P. March (University of California Press, Berkley, 1980), p. 658.
[8]D. E. Grady and R. L. Moody, "Shock compression profiles in ceramics," Technical Report No. SAND96-0551, Sandia National Laboratories, 1996.
[9]T. J. Vogler, W. D. Reinhart, and L. C. Chhabildas, J. Appl. Phys. **95**, 4173 (2004).
[10]Y. Zhang, T. Mashimo, Y. Uemura, M. Uchino, M. Kodama, K. Shibata, K. Fukuoka, M. Kikuchi, T. Kobayashi, and T. Sekine, J. Appl. Phys. **100**, 113536 (2006).
[11]G. I. Kanel, E. B. Zaretsky, A. M. Rajendran, S. V. Razorenov, A. S. Savinykh, and V. Paris, Int. J. Plast. **25**, 649 (2009).
[12]V. Domnich, S. Reynaud, R. A. Haber, and M. Chhowalla, J. Am. Ceram. Soc. **94**, 3605 (2011).
[13]M. Chen, J. W. McCauley, and K. J. Hemker, Science **299**, 1563 (2003).
[14]X. Q. Yan, Z. Tang, L. Zhang, J. J. Guo, C. Q. Jin, Y. Zhang, T. Goto, J. W. McCauley, and M. W. Chen, Phys. Rev. Lett. **102**, 075505 (2009).
[15]K. M. Reddy, P. Liu, A. Hirata, T. Fujita, and M. W. Chen, Nat. Commun. **4**, 2483 (2013).
[16]P. Dera, M. H. Manghnani, A. Hushur, Y. Hu, and S. Tkachev, J. Solid State Chem. **215**, 85 (2014).
[17]S. Aryal, P. Rulis, and W. Y. Ching, Phys. Rev. B **84**, 184112 (2011).
[18]D. E. Taylor, J. W. McCauley, and T. W. Wright, J. Phys. Condens. Matter **24**, 505402 (2012).
[19]D. E. Taylor, J. Am. Ceram. Soc. **98**, 3308 (2015).
[20]E. Betranhandy, N. Vast, and J. Sjakste, Solid State Sci. **14**, 1683 (2012).
[21]Q. An, W. A. Goddard, and T. Cheng, Phys. Rev. Lett. **113**, 095501 (2014).
[22]P. Korotaev, P. Pokatashkin, and A. Yanilkin, Model. Simul. Mater. Sci. Eng. **24**, 015004 (2016).
[23]P. Korotaev, P. Pokatashkin, and A. Yanilkin, Comput. Mater. Sci. **121**, 106 (2016).
[24]Q. An and W. A. Goddard, Phys. Rev. Lett. **115**, 105501 (2015).
[25]X. Yang, S. P. Coleman, J. C. Lasalvia, W. A. Goddard, and Q. An, ACS Appl. Mater. Interfaces **10**, 5072 (2018).
[26]G. R. Johnson and T. J. Holmquist, "A computational constitutive model for brittle materials subjected to large strains, high strain rates and high pressures," in *Shock-Wave and High-Strain-Rate Phenomena in Materials* (Marcel Dekker Inc., New York, 1992), pp. 1075–1081.
[27]G. R. Johnson and T. J. Holmquist, AIP Conf. Proc. **309**, 981 (1994).
[28]G. R. Johnson, T. J. Holmquist, and S. R. Beissel, J. Appl. Phys. **94**, 1639 (2003).
[29]G. R. Johnson and T. J. Holmquist, J. Appl. Phys. **85**, 8060 (1999).
[30]T. J. Holmquist and G. R. Johnson, J. Appl. Phys. **100**, 093525 (2006).
[31]A. N. Parshikov and S. A. Medin, J. Comput. Phys. **180**, 358 (2002).
[32]J. K. Dukowicz, J. Comput. Phys. **61**, 119 (1985).
[33]G. R. Johnson and W. H. Cook, Eng. Fract. Mech. **21**, 31 (1985).
[34]M. L. Wilkins, *Computer Simulation of Dynamic Phenomena* (Springer-Verlag Berlin Heidelberg, 1999), p. 266.
[35]G. R. Johnson and T. J. Holmquist, "Some observations on the strength of failed ceramic," in *Advances in Ceramic Armor: A Collection of Papers Presented at the 29th International Conference on Advanced Ceramics and Composites, January 23-28, 2005, Cocoa Beach, Florida*, Ceramic Engineering and Science Proceedings (John Wiley and Sons, Inc., 2008), pp. 3–10.
[36]S. A. Dyachkov, M. S. Egorova, S. A. Murzov, A. N. Parshikov, and V. V. Zhakhovsky, Lobachevskii J. Math. **38**, 893 (2017).
[37]M. S. Egorova, S. A. Dyachkov, A. N. Parshikov, and V. V. Zhakhovsky, "Parallel SPH modeling using dynamic domain decomposition and load balancing displacement of Voronoi subdomains," Comp. Phys. Commun. (in press).